


Molecular Dispersion Spectroscopy Using a Code-Division-Multiplexed Optical Carrier

Justin Wong,^{*} Chathura P. Bandutunga[✉], Priya Singh[✉], Malcolm B. Gray, and Jong H. Chow
Center for Gravitational Astrophysics, College of Science, Australian National University, Acton, Australian Capital Territory 2601, Australia

 (Received 5 January 2023; revised 1 March 2023; accepted 14 March 2023; published 10 April 2023)

A fiber-optic molecular dispersion spectrometer using code-division multiplexing to make simultaneous phase measurements of a hydrogen cyanide ($\text{H}^{13}\text{C}^{14}\text{N}$) $2\nu_3$ -band P10 rovibrational transition at multiple optical frequencies is demonstrated. A second-derivative anomalous dispersion response is digitally synthesized from sets of these concurrent measurements. The synthesized measurement demonstrates 3 orders of magnitude noise suppression relative to individual measurements, has intrinsic wavelength tuning linearization, and a spectroscopic detection limit of $146 \text{ ppb m}/\sqrt{\text{Hz}}$.

DOI: [10.1103/PhysRevApplied.19.044027](https://doi.org/10.1103/PhysRevApplied.19.044027)

I. INTRODUCTION

Molecular dispersion spectroscopy for the optical detection and characterization of anomalous dispersion is a developing field for the interferometric measurement of trace gas concentrations [1]. As a phase-sensitive detection technique, it eliminates the need for baselining or normalization of the spectroscopic signal that is typically required for absorption-spectroscopy methods [2]. Furthermore, dispersion-sensitive methods excel at measuring high concentrations of a target analyte, where absorption techniques, limited by the nonlinear response of the Beer-Lambert law, result in a reduction of sensitivity [3]. This makes dispersion methods favorable for use cases requiring high signal dynamic range and readout linearity, which is the case in the presence of large intensity and path-length fluctuations. Uses of dispersion spectroscopy include open-path sensing [4] and multi-species atmospheric sensing [5], as well as combustion analysis [6]. Here we present a technique for dispersion spectroscopy that uses code-division multiplexing to synthesize a noise-suppressed measurement with integrated wavelength linearization. We experimentally demonstrate a detection sensitivity of $146 \text{ ppb m}/\sqrt{\text{Hz}}$ calibrated with use of a spectroscopic measurement of the $\text{H}^{13}\text{C}^{14}\text{N}$ P10 transition in the $2\nu_3$ rotational-vibrational band.

A common technique in dispersion spectroscopy is the use of heterodyne modulation, which works by generating one or more additional spectral components or sidebands to a laser source, thereby probing the anomalous dispersion phase shift at multiple optical frequencies. By measuring the interference between these fields, which occurs

at the laser modulation frequency, one can recover phase information pertaining to the molecular dispersion, or its derivatives.

While a number of heterodyne absorption techniques, such as frequency-modulation spectroscopy and wavelength-modulation spectroscopy, are also able to extract phase information, the two most-prominent and most-sensitive dispersion-specific techniques are chirped-laser dispersion spectroscopy (CLADS) [7,8] and heterodyne phase-sensitive dispersion spectroscopy (HPSDS) [9]. CLADS uses a phase or intensity modulator to generate rf sidebands on a optical carrier. As the laser is chirped across the dispersion feature, the sidebands experience a phase shift corresponding to the derivative of dispersion, which is encoded as a frequency modulation on the chirp beat note. This technique is well characterized and has been experimentally demonstrated for *in situ* [10] and open-path [11] measurements of gas molecules in the near-infrared region [12] and the mid-infrared region [13]. At the near-infrared wavelengths targeted in this paper, the sensitivity of CLADS reaches $2.7 \text{ ppm m}/\sqrt{\text{Hz}}$. This is comparable to the sensitivity attained by single-pass absorption methods such as frequency-modulation spectroscopy [14], with the advantages of performing a phase measurement instead of an amplitude measurement.

HPSDS [15] is a technique that reduces the optical and signal extraction complexity of CLADs by eliminating the need to frequency chirp the laser. Instead, two rf sidebands generated by an intensity modulator are tuned over the dispersion feature, encoding the dispersion-induced phase shift in the phase of a heterodyne beat note. This method, by careful tuning of mix-down frequencies, also eliminates the associated high-speed rf electronics required to

^{*}justin.wong@anu.edu.au

demodulate the chirp, while also removing the need to account for nonlinearities in the chirp.

In this paper we develop a dispersion-spectroscopy architecture that uses digital interferometry: a pseudorandom-noise (PRN) modulation technique that synthesizes complex interferometric measurements on simple optical hardware, using code-correlation properties to distinguish different optical paths. Our previous implementations of this technique relied on common-path interferometers to achieve noise immunity, and thus required the sample under test to be integrated tightly within the measurement optics [16]. Here our approach differs by our using digital interferometry to independently recover measurements from multiple transits of a common re-entrant optical delay line. With this simplified optical setup, we retain the ability to suppress both laser frequency noise and delay-line path-length noise as they appear as common noise sources in successive round trips of the delay line. Furthermore, this allows precise interferometric measurements with a single optical path, which adds the flexibility to interrogate the measurement sample either in transmission or in reflection and obviates the need for a separate optical reference or local oscillator.

In this manner, we experimentally demonstrate molecular dispersion spectroscopy via a single optical path through a gas cell and achieve a molecular detection sensitivity of 146 ppb m/ $\sqrt{\text{Hz}}$, which is within a factor of 2 of the molecular detection sensitivity of our noise-immune Sagnac-interferometer architecture [16]. With the sideband generation and demodulation decoupled from the gas-sensing optics, this optical topology can achieve a higher degree of flexibility, and enable the optics for the sample under test to be independently modified to fit design requirements of target applications.

II. CODE-DIVISION-MULTIPLEXED RE-ENTRANT INTERFEROMETER

The foundational technique used in this architecture is digitally enhanced heterodyne interferometry (DEHEI), which has been used extensively in ranging and in multiplexing interferometric applications [17,18]. Here, as per the conceptual diagram shown in Fig. 1(a), a laser of frequency ω_l is phase modulated with a DEHEI binary PRN sequence by an electro-optic modulator (EOM) at a modulation depth of π radians. The resultant phase modulation has the effect of pseudorandomly inverting and thus scrambling the optical phase. After propagating through an optical system, the modulated optical signal is correlated with a delayed local copy of the pseudorandom sequence. By use of a delay equal to the transit time of the optical system, DEHEI uses the correlation of the code to recover the signal of interest. Other signals with different delays will be strongly suppressed by the autocorrelation of the PRN sequence, effectively creating a range gate. This allows

multiple optical signals to be multiplexed within a single interferometer, differentiated by their code time of flight.

In this architecture, the modulated DEHEI field is seeded into a re-entrant-delay-line loop with use of a 3-dB coupler, as seen in Fig. 1(a). An acousto-optic modulator (AOM) is placed within the loop such that successive passes of the delay line are frequency shifted by integer multiples of the AOM frequency ω_s . In addition, each successive pass around the loop delays the pseudorandom sequence by the transit time of the loop, allowing pseudorandom code separability of each frequency term. Note, there will also be an unshifted zero-pass field that bypasses the delay line altogether. In this analysis, we consider only the zero (ω_l), first ($\omega_l + \omega_s$), and second ($\omega_l + 2\omega_s$) passes of the delay line. This restriction is reasonable as the cumulative losses through the AOM and the lack of amplification within the delay line mean that subsequent transits contribute negligible optical power to the final readout.

Following the re-entrant delay line, the three fields we consider enter an $\text{H}^{13}\text{C}^{14}\text{N}$ vapor cell, where they experience different phase shifts corresponding to the anomalous dispersion around an $\text{H}^{13}\text{C}^{14}\text{N}$ molecular transition. This is depicted in Fig. 1(b). Thus, when the three fields are incident on the photodetector, the differential dispersion between the three fields will be carried on the phase of the heterodyne beat notes at ω_s and $2\omega_s$. As the laser frequency ω_l is tuned across the transition, which can be achieved by thermal tuning of the laser, we can write the frequency-dependent phase shifts experienced by each of the fields as per Eqs. (1)–(3):

$$\phi_0 = \frac{\omega_l n(\omega_l) L_{\text{cell}}}{c} + m(t - \tau_0), \quad (1)$$

$$\phi_1 = \left[\frac{(\omega_l + \omega_s) n(\omega_l + \omega_s) L_{\text{cell}}}{c} + \phi_{\text{laser}} \right] + m(t - \tau_1), \quad (2)$$

$$\phi_2 = \left[\frac{(\omega_l + 2\omega_s) n(\omega_l + 2\omega_s) L_{\text{cell}}}{c} + 2\phi_{\text{laser}} \right] + m(t - \tau_2),$$

$$m(t) \in [0, \pi], \quad (3)$$

where ϕ_{laser} is the differential path-length phase noise induced by the laser frequency noise, ω_l is the center frequency of the laser, ω_s is the frequency shift induced by the AOM, $n(\omega)$ is the frequency-dependent refractive index of the $\text{H}^{13}\text{C}^{14}\text{N}$ sample, and L_{cell} is the length of the vapor cell. We write the DEHEI phase modulation as $m(t)$, which pseudorandomly toggles between 0 and π and is time shifted corresponding to the delays τ_0 , τ_1 , and τ_2 experienced by the three optical fields, respectively. We also

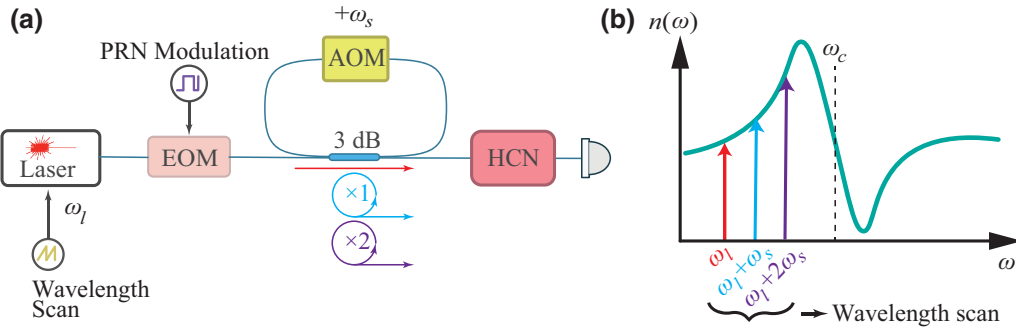


FIG. 1. (a) A conceptual diagram demonstrating the basic optical architecture of the spectrometer. An optical source, with frequency ω_l with linewidth much narrower than an $\text{H}^{13}\text{C}^{14}\text{N}$ molecular transition is split by a 3-dB coupler and seeded into a frequency-shifting re-entrant-delay-line loop. An AOM with frequency shift ω_s is used to provide this frequency shift. There is prompt transmission through the coupler bypassing the loop. This field has the unshifted frequency ω_l . Successive passes through the loop are frequency shifted to $\omega_l + q\omega_s$, where q is the number of loop transits. The three fields illustrated exit the re-entrant loop and enter a vapor cell containing hydrogen cyanide ($\text{H}^{13}\text{C}^{14}\text{N}$), where they experience differential phase shifts corresponding to the anomalous dispersion around an $\text{H}^{13}\text{C}^{14}\text{N}$ transition, as shown in (b).

note that the phase noise scales as the integer multiple of the loop passes, hence the factor of 2 in front of the phase-noise term in Eq. (3). At the photodetector, the three fields, with their respective phase shifts can be written as per Eqs. (4)–(6):

$$E_0 = \frac{E}{2} \alpha(\omega_l) \exp [i\omega_l t + i\phi_0] P(t - \tau_0), \quad (4)$$

$$E_1 = \frac{E}{4} \alpha(\omega_l + \omega_s) \exp [i(\omega_l + \omega_s)t + i\phi_1] \times P(t - \tau_1), \quad (5)$$

$$E_2 = \frac{E}{8} \alpha(\omega_l + 2\omega_s) \exp [i(\omega_l + 2\omega_s)t + i\phi_2] \times P(t - \tau_2), \quad (6)$$

$$P(t) \in [1, -1],$$

where $\alpha(\omega)$ is the frequency-dependent absorption coefficient. The DEHEI phase-modulation term $m(t)$ in Eqs. (1)–(3) is mathematically equivalent to multiplying the field by 1 or -1 . Thus, we factor the DEHEI modulation out of the phase term and rewrite the modulation as a bipolar sequence: $P(t)$. The sum of these fields incident on a square-law photodetector results in a signal with six terms: three dc terms, two terms with heterodyne frequency equal to the AOM frequency, ω_s , and one term with a heterodyne frequency double the AOM frequency, $2\omega_s$. We first write the three dc terms, I_{dc} , in compact form:

$$\sum_{n=0}^2 E_n^2 P^2(t - \tau_n). \quad (7)$$

The two terms interference for between E_0 and E_1 and between E_1 and E_2 are written, respectively, as $I_{\omega,1}$ and $I_{\omega,2}$:

$$I_{\omega,1} \propto \frac{E^2}{4} \alpha(\omega) \alpha(\omega_l + \omega_s) \cos(\omega_s t + \phi_1 - \phi_0) \times P(t - \tau_0) P(t - \tau_1), \quad (8)$$

$$I_{\omega,2} \propto \frac{E^2}{16} \alpha(\omega_l + \omega_s) \alpha(\omega_l + 2\omega_s) \cos(\omega_s t + \phi_2 - \phi_1) \times P(t - \tau_1) P(t - \tau_2). \quad (9)$$

Finally, the $P_{2\omega}$ term is written as follows:

$$I_{2\omega} \propto \frac{E^2}{8} \alpha(\omega_l) \alpha(\omega_l + 2\omega_s) \cos(2\omega_s t + \phi_2 - \phi_0) \times P(t - \tau_0) P(t - \tau_2). \quad (10)$$

For the spectroscopic readout described here, we isolate the two interference terms [Eqs. (8) and (9)]. Since these two terms have the same heterodyne frequency, conventionally, it would not be possible to separately extract the phase carried on each of these heterodyne terms. However, since they have been tagged with DEHEI phase modulation, by correlating them with the appropriately delayed code pairs $P(t - \tau_0)P(t - \tau_1)$ and $P(t - \tau_1)P(t - \tau_2)$, we can isolate these terms in two separate channels.

We then proceed with the standard method of in-phase and quadrature demodulation in heterodyne interferometry, demodulating Eqs. (8) and (9) by mixing down the photodetector voltage signal with a local oscillator phase locked to the AOM frequency ω_s , low-pass filtering, and then calculating the arctangent to recover the phase angle.

We thus extract the differential phases $\Phi_1 = \phi_1 - \phi_0$ and $\Phi_2 = \phi_2 - \phi_1$, noting that these phases will still include the laser phase-noise term ϕ_{laser} . However, by taking the difference between these two expressions, we can form the combination ϕ_{sig} , which allows the cancellation of the common laser phase noise:

$$\begin{aligned}\phi_{\text{sig}} &= (\phi_2 - \phi_1) - (\phi_1 - \phi_0) \\ &= \frac{L_{\text{cell}}}{c} [(\omega_l + 2\omega_s)n(\omega_l + 2\omega_s) - 2(\omega_l \\ &\quad + \omega_s)n(\omega_l + \omega_s) + \omega_l n(\omega_l)] \\ &\approx \frac{\omega_l L_{\text{cell}}}{c} [n(\omega_l + 2\omega_s) - 2n(\omega_l + \omega_s) + n(\omega_l)].\end{aligned}\quad (11)$$

Noting that the AOM frequency shift of 200 MHz is 6 orders of magnitude smaller than the optical frequency of the laser (193 THz) $\omega_s \ll \omega_l$, we have simplified and collected the ω_l frequency term. The form of this expression is equivalent to the definition of the second derivative of the refractive index. Intuitively, we can infer this as ϕ_{sig} is formed by our taking the difference between two phase differences.

III. EXPERIMENTAL IMPLEMENTATION

The experimental demonstration, shown in Fig. 2, uses a Koheras X15 fiber laser with 100-Hz linewidth. To interrogate the full width of the dispersion profile, the laser frequency is thermally tuned with use of the X15 control software. The laser output is phase modulated with a binary PRN modulation using an iXBlue MPX-LN0.1 EOM. The PRN modulation generates an optical spread spectrum, centered at the laser frequency, with characteristic nulls at the PRN symbol (chip) frequency of 16 MHz.

The spread-spectrum optical field is coupled into a fiber re-entrant delay line with use of a 3-dB coupler. The delay line consists of a 30-m potted fiber coil and a fiber-coupled Gooch & Housego FiberQ AOM. This is used to frequency shift successive round trips of the re-entrant delay line by the AOM drive frequency of 200 MHz. The output of the re-entrant delay line is connected to a fiber-coupled vapor cell containing pure $\text{H}^{13}\text{C}^{14}\text{N}$ gas manufactured by Wavelength References (model number HCN-13-C-10). The cell has a pressure of 10 Torr at room temperature, and a path length of 16.5 cm. After interacting with the vapor cell, the resulting interference signal is incident on a fiber-coupled New Focus 1611 photodetector with 1-GHz bandwidth.

Digital signal processing for the system is handled with a National Instruments platform consisting of a Virtex-5 field-programmable gate array (FPGA) coupled with an NI5781 transceiver module, consisting of two differential-output digital-to-analog converters at 100 megasamples per second and two differential-input analog-to-digital converters (ADCs) at 100 megasamples per second. The analog front end of the ADCs additionally has a seventh-order elliptical low-pass antialiasing filter with a 3-dB corner frequency at 40 MHz.

The FPGA system is firstly used for the generation of the PRN modulation. This is output from the digital-to-analog converter at the 16-MHz symbol frequency to drive the EOM. The modulation is also digitally delayed internally on the FPGA and used for demodulation of the three optical delays from the system. These delays correspond to the prompt (τ_0), first (τ_1), and second (τ_2) round trips through the re-entrant delay line.

The AOM is driven at 200 MHz with use of a Liquid Instruments Moku:Pro signal generator that is phase locked to the National Instruments FPGA system. The frequency offset from the AOM center frequency

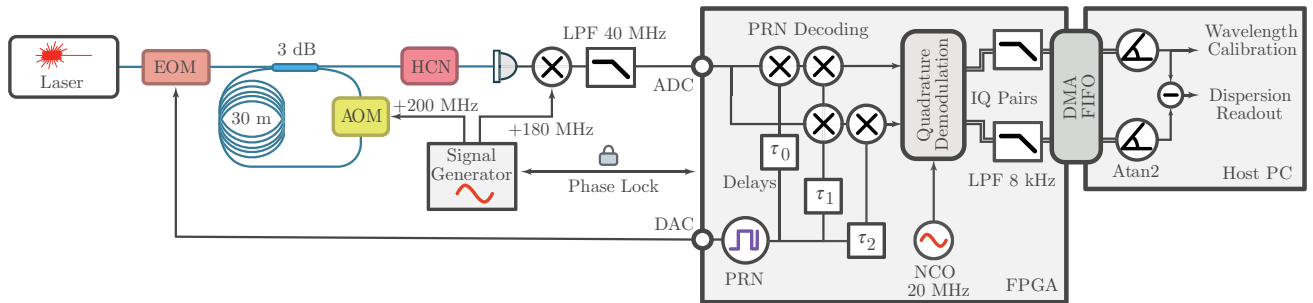


FIG. 2. The output of a 1550-nm fiber laser is phase modulated by an EOM to encode a PRN sequence. This is seeded into a re-entrant frequency-shifting loop consisting of a 30-m-long fiber coil and a 200 MHz AOM. There is a prompt path through the loop coupler bypassing the loop that does not experience a frequency shift, a single pass around the loop that experiences a 200-MHz shift, and a double pass that experiences a 400-MHz shift. The three fields experience differential phase shifts as they interrogate the dispersion profile of an $\text{H}^{13}\text{C}^{14}\text{N}$ vapor cell, and a photodetector records the resulting interference. To scan the dispersion profile, the laser wavelength is swept across the $\text{H}^{13}\text{C}^{14}\text{N}$ transition by thermal tuning. Atan2, two-argument arctangent; DAC, digital-to-analog converter; DMA, direct memory access; FIFO, first in first out; IQ, in-phase and quadrature; LPF, low-pass filter; NCO, numerically controlled oscillator; PC, personal computer.

(200 MHz) is used to tune the DEHEI heterodyne frequency for optimal crosstalk rejection [19].

The voltage signal from the New Focus 1611 photodetector is first mixed down by a 180-MHz tone phase locked to the 200-MHz tone used to drive the AOM. The down-mixing is performed with a Minicircuits ZP-3MH+ mixer to meet the 40-MHz-bandwidth requirement of the ADC on the FPGA. We choose a local-oscillator frequency of 180 MHz, which is mixed with the heterodyne beat note at 200 MHz, thus placing the 20-MHz mixed-down output squarely in the middle of the ADC bandwidth. The resulting 20-MHz intermediate frequency is digitized by the ADC on the FPGA and then correlated with the appropriately delayed codes.

Following code correlation, the two demultiplexed channels corresponding to Eqs. (8) and (9) are mixed with a numerically controlled oscillator at 20 MHz and low pass filtered to recover the in-phase and quadrature projections relative to the numerically controlled oscillator. These two in-phase and quadrature pairs are low pass filtered and decimated to 8 kHz to remove high-frequency upshifted components and then streamed onto a host personal computer, where a two-argument arctangent is computed to recover the phases of the two channels. Finally, the recovered differential phases are subtracted to obtain the double-derivative spectroscopic readout.

IV. SELF-CALIBRATION AND SENSITIVITY

The individual phases of the two measurement channels can be used to perform a calibration of the wavelength scan. As the laser is thermally tuned across the transition, the re-entrant delay line causes each channel to accumulate a phase shift at a rate proportional to the rate of frequency tuning. Since 2π radians of phase corresponds to one free spectral range (FSR) of the re-entrant delay line, by measuring the FSR, we can convert the accumulated phase to laser-frequency detuning relative to the absorption line. This is shown in Fig. 3(a), where a slight concave nonlinearity in the wavelength scan can be seen. This calibration curve is then used to reparameterize the time axis in the unit of frequency, thus removing the nonlinearity of thermal tuning from our measurement. As an example, we perform this calibration on the absorption profile of the $\text{H}^{13}\text{C}^{14}\text{N}$ transition in Fig. 3(b), converting a time-domain trace of the absorption line into frequency.

To determine the sensitivity of the spectroscopic phase measurement, a 10-min off-resonance measurement is taken where the laser is thermally tuned away from the transition, measuring solely the intrinsic noise of the phase measurement. From this, we compute the noise floor as determined by the off-resonance phase spectral density of the two channels, and their subtraction, which forms the spectroscopic readout. The two individual channels as well as their subtraction are shown in Fig. 4. The subtracted

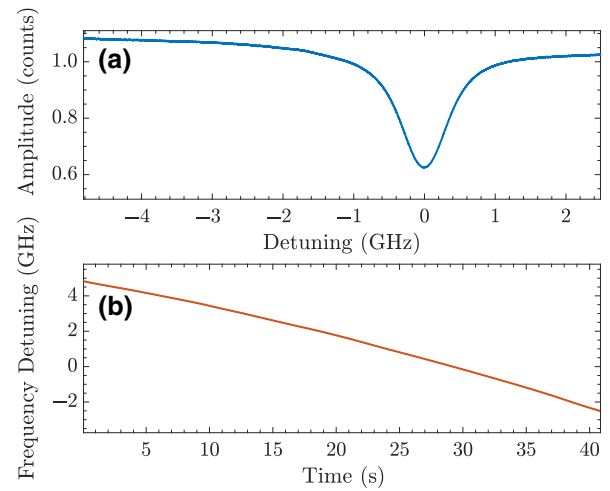


FIG. 3. Wavemeter-calibration comparison. (a) The phase accrued by the re-entrant delay line as the laser is thermally tuned over the transition over 40 s. This is converted to frequency with use of *a priori* knowledge of the re-entrant-delay-line FSR as computed from the fiber-coil length. (b) The frequency calibration is used to remap the measured absorption from time to frequency.

readout shows a minimum noise floor of $8 \mu\text{rad}/\sqrt{\text{Hz}}$, along with a shelf below 10 Hz, while the phase noise of the individual channels display a $1/f$ roll-up below 10 Hz. At 10 mHz, this results in 5 orders of magnitude of suppression in phase noise, indicating that the subtraction strongly suppresses laser phase noise. The shelf is caused by re-entrant code noise, as seen in previous implementations of re-entrant delay lines, which can be addressed in future implementations with use of a calibrated FSR scan [20].

V. SPECTROSCOPIC MEASUREMENT

To validate the measurement scheme, we perform a spectroscopic measurement of the P10 line in the $2\nu_3$ rotational-vibrational band of $\text{H}^{13}\text{C}^{14}\text{N}$, a common wavelength reference for 1550 nm. The measured spectroscopic signal is shown in Fig. 5(a). The gas cell used contains pure $\text{H}^{13}\text{C}^{14}\text{N}$ gas at a calibrated pressure of 10 Torr and is interrogated by our thermally tuning the X15 laser over the transition. With these vapor-cell parameters, the peak absorption of the P10 transition in the vapor cell is calculated to be 0.7 with use of data from the GEISA2003 spectroscopic database [21]. The double-differential readout is converted from time to optical frequency shift with use of a single round-trip measurement to remove nonlinearities in the thermal tuning rate, and the readout is low pass filtered from a readout rate of 7.8 kHz to 10 Hz to remove high-frequency technical noise from the measurement.

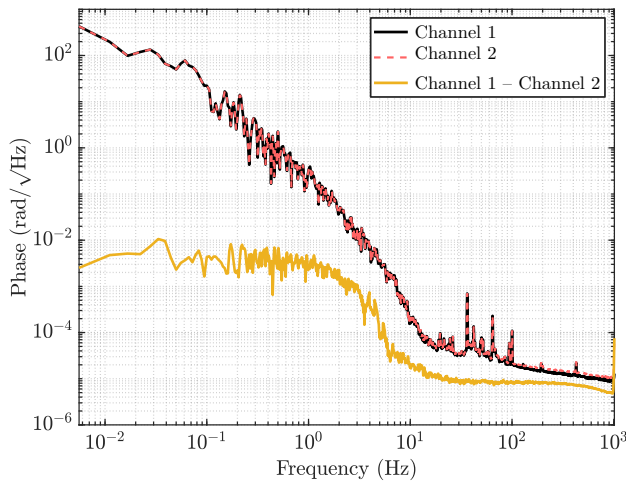


FIG. 4. The phase readouts from the two individual channels, and their subtraction. The subtraction, which forms the spectroscopic readout, demonstrates strong suppression of up to 5 orders of magnitude for $1/f$ phase noise below 10 Hz. The low-frequency noise shelf in the subtracted measurement is due to code noise [20].

Using the known pressure, temperature, and concentration of the cell, we compute a theoretical Voigt line shape with a floating line center. We then compute the dispersion by performing a numerical Hilbert transform [22]. Using the dispersion, we model the expected double-differential readout, which is then overlaid on the experimental data in Fig. 5(a). The modeled signal shows good agreement with the experimentally obtained signal, with the residuals plotted in Fig. 5(b).

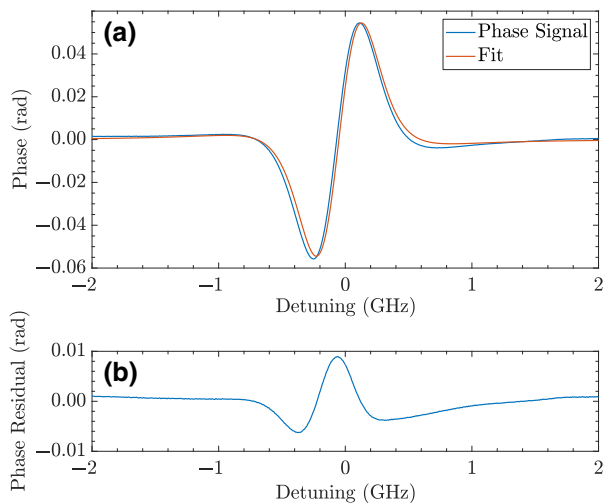


FIG. 5. (a) The experimental phase signal, and the theoretical phase signal generated from the model using experimental pressure and temperature conditions. The x axis is shifted such that the phase signal is centered at the line center of the P10 transition. (b) The residuals between the measurement and the fit.

To determine the concentration sensitivity of this technique, we refer back to the phase-noise spectral density shown in Fig. 4, where the phase sensitivity above 30 Hz is measured to be $8 \mu\text{rad}/\sqrt{\text{Hz}}$. This phase sensitivity can be converted to concentration in the unit of parts per billion meters (ppb m) by our noting that the peak phase excursion of 120 mrad measured in Fig. 5 occurs at a vapor cell concentration of 2185 ppm m. This sets a calibration factor of 18 ppm m/mrad. Since the spectroscopic phase signal scales linearly with concentration, we can readily convert our phase-noise spectral density by this calibration to give a concentration sensitivity in the unit of parts per billion meters per square-root hertz (ppb m/ $\sqrt{\text{Hz}}$). In performing this calibration, we arrive at a noise-equivalent detection limit of $146 \text{ ppb m}/\sqrt{\text{Hz}}$, which exceeds the sensitivity of frequency-modulation spectroscopy and wavelength-modulation spectroscopy in the near-infrared region with single-pass gas cells by a factor of 3 [14], and is comparable to the concentration sensitivity achieved by CLADS and HPSDS [15]. This is equivalent to a fractional absorption sensitivity of $4.9 \times 10^{-5}/\sqrt{\text{Hz}}$.

The detection limit is a factor of 2 less than that achieved by our previous work in dispersion spectroscopy using a Sagnac interferometer [16]. However, the method described in this paper affords greater flexibility in that the spectroscopic sample is placed unidirectionally, in line with the fiber delay loop, instead of being embedded within a bidirectional Sagnac loop. Therefore, this single-pass approach allows easier alignment for spectroscopic measurements using free-space cells. We also highlight the ability (with the addition of a circulator) to obtain a dispersion signal in reflection in addition to transmission. With this slight modification in the setup layout, this architecture can thus be used as an optical network analyzer to characterize a wide array of photonic components, such as fiber Bragg gratings, filters, and dichroic mirrors.

VI. CONCLUSION

In this paper, we present and experimentally verify a molecular dispersion spectroscopy technique using a code-division-multiplexed optical carrier. We demonstrate good agreement between experimental measurements and a theoretical phase signal computed with an analytical model.

With synthesized common-mode suppression of laser and path-length phase noise by up to 5 orders of magnitude, the system demonstrates a noise-equivalent concentration detection limit of $146 \text{ ppb m}/\sqrt{\text{Hz}}$. Given the sub-parts-per-million detection limit, the architecture offers a robust, optically simple, and flexible metrology scheme that can be readily adapted to the requirements of different sensing configurations.

ACKNOWLEDGMENTS

This research is supported by an Australian Government Research Training Program Scholarship.

-
- [1] M. Nikodem and G. Wysocki, Chirped laser dispersion spectroscopy for remote open-path trace-gas sensing, *Sensors (Basel, Switzerland)* **12**, 16466 (2012).
- [2] A. L. Chakraborty, K. Ruxton, W. Johnstone, M. Lengden, and K. Duffin, Elimination of residual amplitude modulation in tunable diode laser wavelength modulation spectroscopy using an optical fiber delay line, *Opt. Express* **17**, 9602 (2009).
- [3] M. Nikodem and G. Wysocki, Measuring optically thick molecular samples using chirped laser dispersion spectroscopy, *Opt. Lett.* **38**, 3834 (2013).
- [4] M. Nikodem, G. Plant, D. Sonnenfroh, and G. Wysocki, Open-path sensor for atmospheric methane based on chirped laser dispersion spectroscopy, *Appl. Phys. B* **119**, 3 (2015).
- [5] S. Paul, P. Martín-Mateos, N. Heermeier, F. Küppers, and P. Acedo, Multispecies heterodyne phase sensitive dispersion spectroscopy over 80 nm using a MEMS-VCSEL, *ACS Photon.* **4**, 2664 (2017).
- [6] L. Ma, Z. Wang, K.-P. Cheong, H. Ning, and W. Ren, Mid-infrared heterodyne phase-sensitive dispersion spectroscopy in flame measurements, *Proc. Combust. Inst.* **37**, 1329 (2019).
- [7] G. Wysocki and D. Weidmann, Molecular dispersion spectroscopy for chemical sensing using chirped mid-infrared quantum cascade laser, *Opt. Express* **18**, 26123 (2010).
- [8] M. Nikodem and G. Wysocki, Molecular dispersion spectroscopy - new capabilities in laser chemical sensing: Molecular dispersion spectroscopy, *Ann. N. Y. Acad. Sci.* **1260**, 101 (2012).
- [9] P. Martín-Mateos, B. Jerez, and P. Acedo, Heterodyne architecture for tunable laser chirped dispersion spectroscopy using optical processing, *Opt. Lett.* **39**, 2611 (2014).
- [10] P. Martín-Mateos, B. Jerez, and P. Acedo, Dual electro-optic optical frequency combs for multiheterodyne molecular dispersion spectroscopy, *Opt. Express* **23**, 21149 (2015).
- [11] M. Nikodem, Chirped laser dispersion spectroscopy for laser-based hydrogen sulfide detection in open-path conditions, *Opt. Express* **24**, A878 (2016).
- [12] Y. Chen, M. Soskind, J. McSpirtt, J. Liu, R. Wang, N. Li, X. Guo, M. A. Zondlo, and G. Wysocki, Fugitive methane detection using open-path stand-off chirped laser dispersion spectroscopy, *Opt. Lett.* **46**, 3005 (2021).
- [13] G. Wysocki and D. Weidmann, Molecular dispersion spectroscopy for chemical sensing using chirped mid-infrared quantum cascade laser, *Opt. Express* **18**, 26123 (2010).
- [14] F. Wang, S. Jia, Y. Wang, and Z. Tang, Recent developments in modulation spectroscopy for methane detection based on tunable diode laser, *Appl. Sci.* **9**, 2816 (2019).
- [15] P. Martín-Mateos and P. Acedo, Heterodyne phase-sensitive detection for calibration-free molecular dispersion spectroscopy, *Opt. Express* **22**, 15143 (2014).
- [16] J. Wong, C. P. Bandutunga, Y. Zhang, M. B. Gray, and J. H. Chow, Digitally enhanced molecular dispersion spectroscopy, *Opt. Lett.* **45**, 6290 (2020).
- [17] D. A. Shaddock, Digitally enhanced heterodyne interferometry, *Opt. Lett.* **32**, 3355 (2007).
- [18] Y. Zhang, C. P. Bandutunga, M. B. Gray, and J. H. Chow, Multi-target CW interferometric acoustic measurements on a single optical beam, *Opt. Express* **27**, 18477 (2019).
- [19] P. G. Sibley, R. L. Ward, L. E. Roberts, S. P. Francis, and D. A. Shaddock, Crosstalk reduction for multi-channel optical phase metrology, *Opt. Express* **28**, 10400 (2020).
- [20] S. Ngo, D. A. Shaddock, T. G. McRae, T. T.-Y. Lam, J. H. Chow, and M. B. Gray, Suppressing Rayleigh backscatter and code noise from all-fiber digital interferometers, *Opt. Lett.* **41**, 84 (2016).
- [21] N. Jacquinet-Husson, *et al.*, The 2003 edition of the GEISA/IASI spectroscopic database, *J. Quant. Spectrosc. Radiat. Trans.* **95**, 429 (2005).
- [22] K. A. Whittaker, J. Keaveney, I. G. Hughes, and C. S. Adams, Hilbert transform: Applications to atomic spectra, *Phys. Rev. A* **91**, 032513 (2015).